Numerical Simulation of High-Incidence Flow over the Isolated F-18 Fuselage Forebody

Lewis B. Schiff,* Russell M. Cummings,† Reese L. Sorenson,‡ and Yehia M. Rizk‡
NASA Ames Research Center, Moffett Field, California 94035

As part of the NASA High Alpha Technology Program, fine-grid Navier-Stokes solutions have been obtained for flow over the fuselage forebody and wing leading-edge extension of the F/A-18 high alpha research vehicle at large incidence. The resulting flows are complex, and exhibit crossflow separation from the sides of the forebody and from the leading edge extension. A well-defined vortex pattern is observed in the leeward-side flow. Results obtained for laminar flow show good agreement with flow visualizations obtained in ground-based experiments. Further, turbulent flows computed at high-Reynolds-number flight-test conditions show good agreement with surface and offsurface visualizations obtained in flight.

Introduction

A HIGH alpha technology program is currently underway within NASA. The objectives of the program include the development of flight-validated design methods that accurately predict the aerodynamics and flight dynamics of aircraft maneuvering in the high-angle-of-attack regime. In addition, the program goals include the development of aerodynamic control concepts that can improve the maneuverability of current and future aircraft. Toward meeting these objectives, the program integrates ground-based experimental and computational investigations underway at the NASA Ames, NASA Langley, and NASA Lewis Research Centers, with flight-test investigations being conducted on the F/A-18 high alpha research vehicle (HARV) at the NASA Ames-Dryden Flight Research Facility. These tests include surface and offsurface visualization, as well as quantitative measurements, of the flow surrounding the HARV at large incidence. This paper presents initial results of Navier-Stokes computations of the flow about the fuselage forebody and wing leading-edge extension of the F-18 HARV at conditions matching those of the flight tests. Parallel computational efforts conducted at NASA Langley are reported in Refs. 1 and 2.

Numerical prediction of the flow over aircraft flying at large angles of attack is a difficult aerodynamic problem. High-angle-of-attack flows contain large regions of three-dimensional separated flow, where the boundary layers leave the surface of the body along surfaces of separation, and roll up on the leeward side of the body to form strong concentrated vortical flows (see Fig. 1, which shows vortical flow about an F-18 visualized by natural flow condensation). Separated flows have historically been treated by a wide variety of computational methods, ranging from potential flow methods, vortex cloud methods, inviscid panel methods incorporating free shear layers, Euler methods, and most recently, parabolized Navier-Stokes (PNS) and time-marching Navier-Stokes techniques. In addition, a variety of combined inviscid/viscous techniques (potential/boundary-layer or Euler/boundary-layer techniques) have been utilized. However, the close coupling that exists between the strength and location of the leeward vortical flow and the location of the viscous layer separation lines has precluded accurate predictions of high-incidence flow with the more approximate techniques.

The recent introduction of supercomputers such as the CRAY-2 has permitted a quantum increase in the size of computational grids. As a result, it is now possible to compute high-angle-of-attack flows over bodies and aircraft components with codes based on the Reynolds-averaged Navier-Stokes equations and using sufficient grid points to adequately resolve the main features of the three-dimensional separated flowfield (cf. Refs. 3–10). In conjunction with this increase in computer capability, effective numerical tools are being developed that properly model the fundamental fluid dynamic processes occurring at high angles of attack. Consequently, we have focused solely on time-marching Navier-Stokes computations, and have used the three-dimensional partially flux-split Navier-Stokes code reported by Steger et al.[11] Several of the more important numerical and physical concerns that must be addressed for accurate numerical predictions of high-incidence flows have been identified and discussed in a recent work.[12] The end result will be a set of numerical tools that will enable researchers to confidently predict flow over aircraft at high angles of attack.

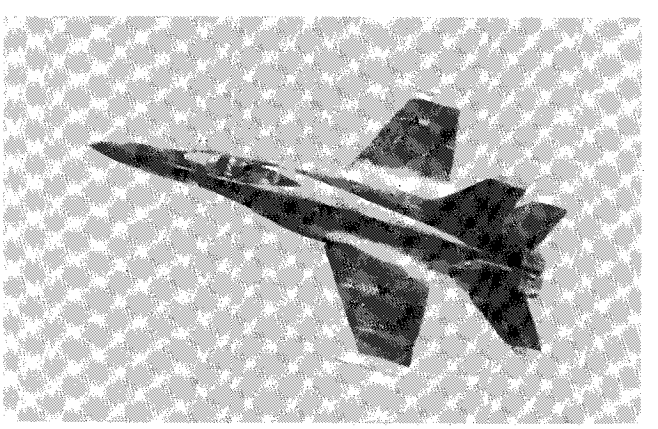

Fig. 1 Leading-edge extension vortices on F-18 visualized by natural condensation.

Presented as Paper 89-0339 at the AIAA 27th Aerospace Sciences Meeting, Reno, NV, Jan. 9–12, 1989; received Feb. 11, 1989; revision received Oct. 15, 1990; accepted for publication Oct. 15, 1990.

*Special Assistant for High Alpha Technology, Fluid Dynamics Division, Mail Stop 258-1. Associate Fellow AIAA.

†National Research Council Research Associate. Associate Professor, on leave from California Polytechnic State University, Aeronautical Engineering Department, San Luis Obispo, CA 93407. Senior Member AIAA.

‡Research Scientist, Applied Computational Fluids Branch. Member AIAA.

Theoretical Background

Governing Equations

The conservation equations of mass, momentum, and energy can be represented in a flux-vector form that is convenient for numerical simulations as[13]

$$\partial_\tau \hat{Q} + \partial_\xi (\hat{F} + \hat{F}_v) + \partial_\eta (\hat{G} + \hat{G}_v) + \partial_\zeta (\hat{H} + \hat{H}_v) = 0 \quad (1)$$

where τ is the time and the independent spatial variables, ξ, η, and ζ are chosen to map a curvilinear body-conforming grid into a uniform computational space. In Eq. (1), $\hat{Q}$ is the vector of dependent flow variables; $\hat{F} = \hat{F}(\hat{Q})$, $\hat{G} = \hat{G}(\hat{Q})$, and $\hat{H} = \hat{H}(\hat{Q})$ are the inviscid flux vectors, and the terms $\hat{F}_v$, $\hat{G}_v$, and $\hat{H}_v$ are fluxes containing the viscous derivatives. A nondimensional form of the equations is used throughout this work. The conservative form of the equations is maintained chiefly to capture shock waves present in transonic and supersonic flows as accurately as possible.

For body-conforming coordinates and high-Reynolds number flows, if ζ is the coordinate leading away from the surface, the thin-layer approximation can be applied, which yields[14,15]

$$\partial_\tau \hat{Q} + \partial_\xi \hat{F} + \partial_\eta \hat{G} + \partial_\zeta \hat{H} = Re^{-1} \partial_\zeta \hat{S} \quad (2)$$

where only viscous terms in the ζ direction are retained. These have been collected into the vector $\hat{S}$, and the nondimensional Reynolds number Re is factored from the viscous flux term.

In differencing these equations, it is often advantageous to difference about a known base solution denoted by subscript o, as follows

$$\begin{aligned} &\delta_\tau(\hat{Q} - \hat{Q}_o) + \delta_\xi(\hat{F} - \hat{F}_o) + \delta_\eta(\hat{G} - \hat{G}_o) \\ &\quad + \delta_\zeta(\hat{H} - \hat{H}_o) - Re^{-1}\delta_\zeta(\hat{S} - \hat{S}_o) = \\ &\quad -\partial_\tau \hat{Q}_o - \partial_\xi \hat{F}_o - \partial_\eta \hat{G}_o - \partial_\zeta \hat{H}_o + Re^{-1}\partial_\zeta \hat{S}_o \end{aligned} \quad (3)$$

where δ indicates a general difference operator, and ∂ is the differential operator. If the base state is properly chosen, the differenced quantities can have smaller and smoother variation and, therefore, less differencing error. In particular, errors introduced into the solution by the finite-difference approximations of the spatial metrics can be reduced. In the current application, the freestream is used as the base solution and the right-hand side of Eq. (3) is zero.

Turbulence Model

The coefficients of viscosity and thermal conductivity that appear in Eq. (2) are specified from auxiliary relations. For laminar flow, the coefficient of viscosity is obtained using Sutherland's law, whereas for turbulent flow the coefficient is obtained from the eddy-viscosity turbulence model reported by Degani and Schiff.[16] The coefficient of thermal conductivity is obtained, once the viscosity coefficient is known, by assuming a constant Prandtl number.

Degani and Schiff developed a modification to the well-known Baldwin-Lomax[14] model (which is based on the two-layer model reported by Cebeci et al.[17]). As proposed by Baldwin and Lomax, the turbulence model examines a quantity containing the local fluid vorticity magnitude to determine the length scale, and, thus, the eddy viscosity coefficient. The modifications made by Degani and Schiff[16] permit the model to differentiate between the vorticity within the attached boundary layers and the vorticity on the surfaces of separation, and, thus, to select a length scale based on the thickness of the attached boundary layers rather than one based on the radial distance between the body surface and the surface of separation. Thus, the modifications extend the model in a rational manner to permit an accurate determination of the viscous length scale for high-angle-of-attack flows in regions of crossflow separation, where a strong leeward vortical flow structure exists.

Numerical Algorithm

The implicit scheme employed in this study is the F3D algorithm reported by Steger et al. in Ref. 11. The algorithm uses flux-vector splitting[18] to upwind difference the convection terms in one coordinate direction (nominally streamwise). As discussed in Ref. 11, schemes using upwind differencing can have several advantages over methods that utilize central spatial differences in each direction. In particular, such schemes can have natural numerical dissipation and better stability properties. By using upwind differencing for the convective terms in the streamwise direction while retaining central differencing in the other directions, a two-factor implicit approximately factored algorithm is obtained, which has been shown to be unconditionally stable[19] for a representative model wave equation. The scheme may be written for the thin-layer Navier-Stokes equations in the form

$$\begin{aligned} &[I + h\delta_\xi^b(\hat{A}^+)^n + h\delta_\zeta \hat{C}^n - hRe^{-1}\bar{\delta}_\zeta J^{-1}\hat{M}^n J - D_i|_\zeta] \\ &\quad \times [I + h\delta_\xi^f(\hat{A}^-)^n + h\delta_\eta \hat{B}^n - D_i|_\eta]\Delta\hat{Q}^n = \\ &\quad -\Delta t\{\delta_\xi^b[(\hat{F}^+)^n - \hat{F}_\infty^+] + \delta_\xi^f[(\hat{F}^-)^n - \hat{F}_\infty^-] \\ &\quad +\delta_\eta(\hat{G}^n - \hat{G}_\infty) + \delta_\zeta(\hat{H}^n - \hat{H}_\infty) \\ &\quad -Re^{-1}\bar{\delta}_\zeta(\hat{S}^n - \hat{S}_\infty)\} - D_e(\hat{Q}^n - \hat{Q}_\infty) \end{aligned} \quad (4)$$

where $h = \Delta t$ or $\Delta t/2$ for first- or second-order time accuracy, and the freestream base solution is used, denoted by the subscript ∞. Second-order time accuracy is used when a nonsteady solution is required. In Eq. (4), δ is typically a three-point second-order accurate central difference operator, $\bar{\delta}$ is a midpoint operator used with the viscous terms, and the operators δ_ξ^b and δ_ξ^f are backward and forward three-point difference operators. The flux $\hat{F}$ has been split into $\hat{F}^+$ and $\hat{F}^-$, according to the sign of the eigenvalues of the Jacobian matrix,[18] and the matrices, $\hat{A}^\pm$, $\hat{B}$, $\hat{C}$, and $\hat{M}$ result from local linearization of the fluxes about $\hat{F}$, $\hat{G}$, $\hat{H}$, and $\hat{S}$, respectively. Note that J denotes the Jacobian of the coordinate transformation. Dissipation operators D_e and D_i are used in the central space differencing directions. Full details of the development of the algorithm may be found in Refs. 11 and 19.

Numerical Smoothing

The finite-difference scheme[11] uses flux-splitting in the ξ direction and central differencing in the η and ζ directions. As a consequence, numerical dissipation terms denoted by D_i and D_e in Eq. (4) are employed in the η and ζ directions, and are

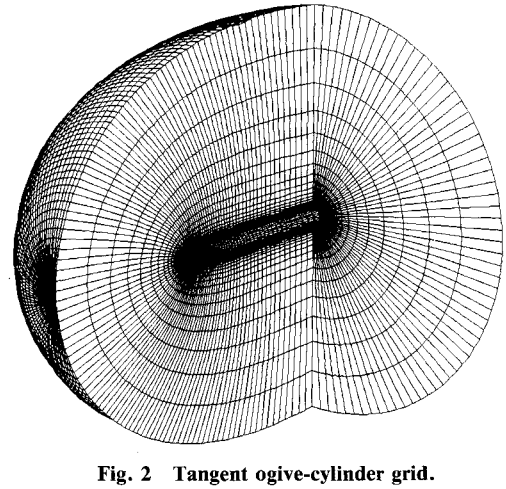

Fig. 2 Tangent ogive-cylinder grid.

combinations of second and fourth differences. The smoothing terms are of the form

$$D_e|_\eta = (\Delta t)J^{-1}\left\{\epsilon_2\bar{\delta}|\hat{B}|\beta\bar{\delta} + \epsilon_4\bar{\delta}\frac{|\hat{B}|}{1+\beta}\bar{\delta}^3\right\}\Big|_\eta J$$
$$D_i|_\eta = (\Delta t)J^{-1}\left\{\epsilon_2\bar{\delta}|\hat{B}|\beta\bar{\delta} + 2.5\epsilon_4\bar{\delta}\frac{|\hat{B}|}{1+\beta}\bar{\delta}^3\right\}\Big|_\eta J \quad (5)$$

where

$$\beta = \frac{|\bar{\delta}^2 p|}{|(1+\bar{\delta}^2)p|}$$

and where $|\hat{B}|$ is the norm of the matrix $\hat{B}$, or an approximation. Here p is the nondimensional fluid pressure and ϵ_2 is $\mathcal{O}(1 + M_\infty{}^\gamma)$ while ϵ_4 is $\mathcal{O}(0.01)$. In this form, the second-order smoothing terms act to control numerical oscillations across shock waves, whereas the fourth-order smoothing is effective elsewhere. To improve the accuracy of the solutions, the fourth-order numerical smoothing terms are further scaled by the nondimensional local velocity ratio, q/q_∞. This has the effect of reducing the numerical smoothing in the viscous layer adjoining the body surface where viscous dissipation controls the dispersion. In this region, large numerical smoothing terms can adversely affect the accuracy of the solution by modifying the physical viscous terms.

Body Geometry and Grid Generation

Ogive-Cylinder Grid

A series of computations was performed for subsonic flow over the ogive cylinder shown in Fig. 2. The body consisted of a 3.5 diam tangent ogive forebody with a 7.0 diam cylindrical afterbody extending aft of the ogive-cylinder junction to $x/D = 10.5$. This configuration was selected for study because an ogive-cylinder body having a 3.5 diam tangent ogive nose and a 4.0 diam cylindrical afterbody had been extensively tested by Lamont[20] in the Ames 12-ft pressure wind tunnel. In that experiment, detailed surface pressure distributions were obtained at Reynolds numbers (based on freestream conditions and cylinder diameter) ranging from $Re_D = 200{,}000$ to $Re_D = 4.0 \times 10^6$, and at angles of attack ranging from $\alpha = 20$ to 90 deg.

The grid used for numerical prediction of the flow about the ogive cylinder is shown in Fig. 2. The flow was assumed to be symmetrical about the angle-of-attack plane, thus a half-body grid and a plane of symmetry boundary condition were used. For flows that are not bilaterally symmetric, a full-body grid and a circumferential continuation condition would be used (cf. Ref. 21). The grid consisted of 61 equispaced circumferential planes ($\Delta\phi = 3$ deg), including the windward and leeward symmetry planes. In each circumferential plane, the grid contained 50 radial points extending between the body surface and the computational outer boundary and 59 axial points between the nose and the rear of the body.

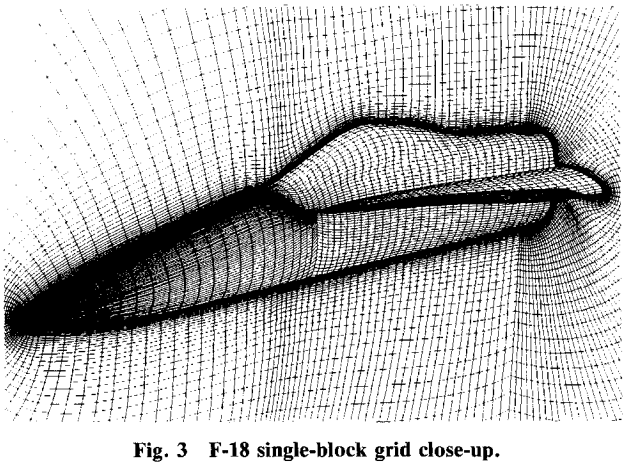

Fig. 3 F-18 single-block grid close-up.

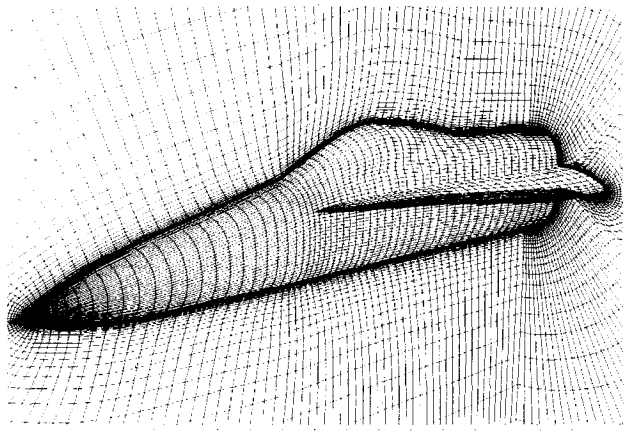

Fig. 4 F-18 two-block grid close-up.

Single-Block F-18 Grid

Computations were performed for the F-18 fuselage forebody and wing leading-edge extension (LEX) using two grid systems. A single-block grid, shown in Fig. 3, was obtained with a hyperbolic grid generation technique,[22] while a two-block grid, shown in Fig. 4, was obtained with an elliptic grid generator.[23] Flow solutions were obtained using the two alternative grid topologies to compare their suitability for computing high-incidence flows about this complex aircraft geometry. As in the ogive-cylinder computations, the flow was assumed to be symmetric about the angle-of-attack plane, and a half-body grid was employed. For flows with nonzero sideslip, a full-body grid and a circumferential periodic continuation condition[21] can be employed. Both grids had a spherical nose tip topology and define the F-18 geometry from the nose to the axial station where the wing joins the body. No attempt was made, in this work, to define the wing or aft fuselage geometry.

The single-block F-18 grid (Fig. 3) was obtained using the hyperbolic generation technique described in detail in Ref. 22. In this method, three simultaneous nonlinear hyperbolic partial differential equations are solved by marching outward from the specified body surface. The generated grid lines emanate orthogonally from the body, while a user-specified cell volume serves to control the resulting grid spacing. The surface grid is also specified by the user. Thus, grid points can be placed and clustered along the body cross sections as required to resolve regions of geometric complexity, or regions where complex flow structures may occur. Because the three-dimensional grid is obtained by marching, the numerical procedure is efficient in terms of computer time and memory. The main disadvantage of the marching procedure is the inability to prescribe an exact location for the outer boundary. However, an approximate location for the outer boundary can be obtained through an appropriate specification of the cell volumes. The resulting grid consisted of 69 axial, 83 circumferential, and 71 radial points.

Two-Block F-18 Grid

Even with the large memory size available on the CRAY-2 computer, it is not practical to develop a single-block grid that includes the geometric complexity of a complete aircraft. Thus, for computations of the full HARV configuration, a multiblock grid will be needed (cf. Refs. 24 and 25 for examples of multiblock Navier-Stokes computations of flow over a complete aircraft configuration in transonic low-incidence flow). In the present computations of flow over the F-18 forebody, the decision to use a two-block grid was strongly influenced by the presence of the relatively large LEX. A large number of circumferential points are necessary to define the rear of the LEX geometry, but a problem arises

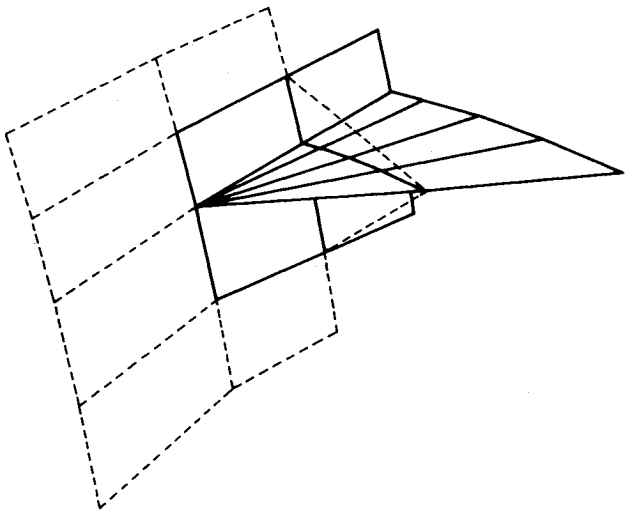

Fig. 5 Details of two-block grid overlap region.

as one moves forward along the body and approaches the point of origin of the LEX (see Figs. 3 and 4). What should be done with those grid points as the physical area of the LEX approaches zero? One possible method, not used in this study, is to allow points to spill from the LEX to the adjoining fuselage one by one as the area decreases. Alternatively, for the one-block grid (Fig. 3), the circumferential points were allowed to converge toward the front of the LEX, and then to expand circumferentially to become equispaced on the fuselage forebody ahead of the LEX.

This gridding difficulty can be alleviated by using a two-block grid. As implemented in this study, the rear grid block starts at the forward end of the LEX. As shown schematically in Fig. 5, all the fore-and-aft lines defining the LEX remain on the LEX as one passes forward, and coalesce into one point at the origin of the LEX. The forward grid block extends one axial plane downstream beyond the origin of the LEX, giving one cell of overlap.

Once the surface grid is specified, the external grid is generated for the region surrounding the body, using the 3DGRAPE program.[23] This is a block-type general purpose elliptic grid generation program, which gives near-orthogonality of the grid near any surface (in this case the body), and allows the user to arbitrarily specify the grid spacing normal to any surface. The forward block consisted of 36 axial points, 51 circumferential points (including the windward and leeward symmetry plane), and 50 radial points. The aft grid block included 32 additional circumferential points to define the LEX geometry, for a total of 35 axial, 83 circumferential, and 50 radial points.

Boundary Conditions and Initial Conditions

Single-Block Grid

The computations performed using the ogive-cylinder and single-block F-18 grids used identical boundary conditions. An adiabatic no-slip condition was applied at the body surface, while undisturbed freestream conditions were maintained at the computational outer boundary. An implicit symmetry plane boundary condition was used at the circumferential edges of the grid, while at the downstream boundary a simple zero-axial-gradient extrapolation was applied. On the upstream spherical axis an extrapolation boundary condition was used to obtain the flow conditions on the axis from the cone of points one axial plane downstream. The flowfield was initially set to freestream conditions throughout the grid, and the flowfield was advanced in time until a steady solution was obtained.

Two-Block Grid

Boundary conditions for the two-block grid topology are identical to those for the single-block grids, except at the common interface. As can be seen in detail in Fig. 5, the front grid block (shown dotted) overlaps the rear block axially by one plane. At the overlap, a direct injection boundary condition is applied. The flow solution is advanced in both blocks concurrently. After the solution is advanced one time step in the front block, flow data from the next-to-last axial plane of the front grid is applied as fixed boundary data at the first axial plane of the rear grid block to advance that solution one step. Analogously, once the flow is advanced one time step in the rear block, flow data at the second axial point of the rear block are applied as fixed boundary data at the last axial point of the front block, and the cycle is repeated.

The direct injection procedure is straightforward to apply, except near circumferential points defining the LEX. As can be seen in Fig. 5, all the circumferential grid points defining the LEX in the rear grid coalesce to one point on the forward grid. Thus, flow conditions at the appropriate circumferential point of the forward block are replicated to provide flow data for the rear block. Conversely, the last axial plane of the front grid has fewer circumferential points than the corresponding second plane of the rear grid. Here, a circumferentially weighted average of the flow values from the rear grid is used to provide flow data for the forward block.

Results and Discussion

Turbulent Flow about the Ogive Cylinder

Comparison with Experiment

To demonstrate the accuracy of numerical predictions obtained with the F3D code for high-incidence flow, a series of

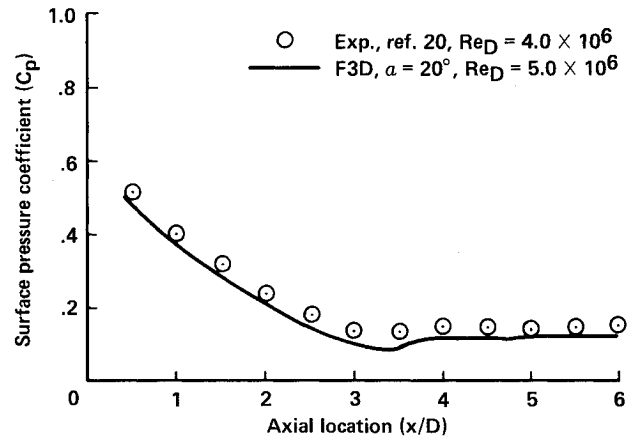

Fig. 6 Longitudinal surface pressure distribution; M_∞ = 0.2, α = 20 deg (turbulent flow).

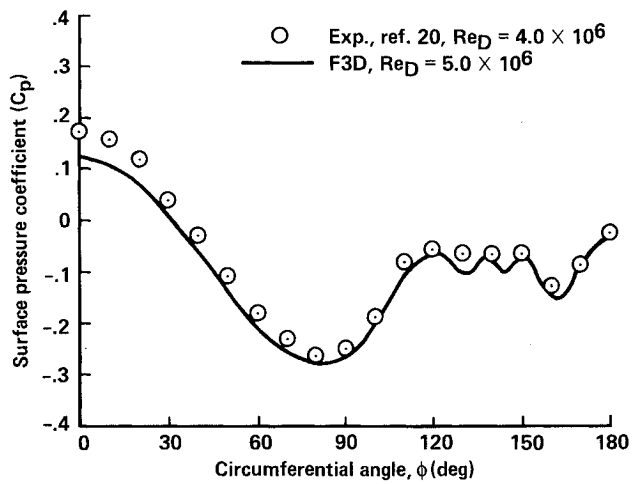

Fig. 7 Circumferential surface pressure distribution at x/D = 6.0; M_∞ = 0.2, α = 20 deg (turbulent flow).

computations for laminar and turbulent flow about the ogive-cylinder body were carried out.[12,21,26] Typical results obtained for the ogive cylinder at $M_\infty = 0.2$, $\alpha = 20$ deg, and $Re_D = 5.0 \times 10^6$ are shown in Figs. 6-8. Figure 6 shows the computed and measured[20] axial surface pressure distributions along the windward plane of symmetry. The analogous comparison for the circumferential surface pressure distributions on the rear of the cylindrical portion of the body ($x/D = 6.0$) is shown in Fig. 7. The computed and measured pressures are in good agreement along the entire length of the body (Fig. 6). The circumferential pressures are compared at a station where a large region of separated flow exists, which is the most difficult region to predict. However, despite the existence of a complex flow structure, the predictions are in good agreement with the experimental data.

The computed surface flow pattern over the forward portion of the body ($0 \leq x/D \leq 6.6$) is presented in Fig. 8. All computations presented in this paper were for a half-body; the resulting solutions were reflected about the symmetry plane in constructing the figures. The surface flow shows existence of both a primary and a secondary crossflow separation line. A tertiary separation line is observed originating toward the rear of the cylindrical body.

Effect of Two-Block Grid

To ensure that the use of a two-block grid and direct injection boundary condition will not degrade the accuracy of the F3D code, the computation discussed above was repeated using a two-block grid. The grid is identical to the one shown in Fig. 2, but was cut and overlapped about the axial grid line at $x/D = 1.80$, and the direct injection boundary condition

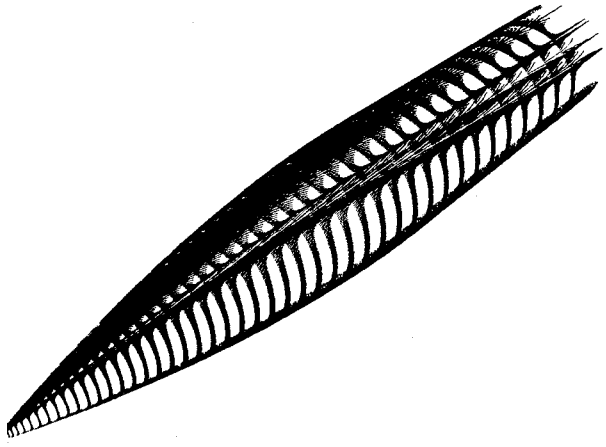

Fig. 8 Surface flow pattern; $M_\infty = 0.2$, $\alpha = 20$ deg, $Re_D = 5.0 \times 10^6$ (turbulent flow).

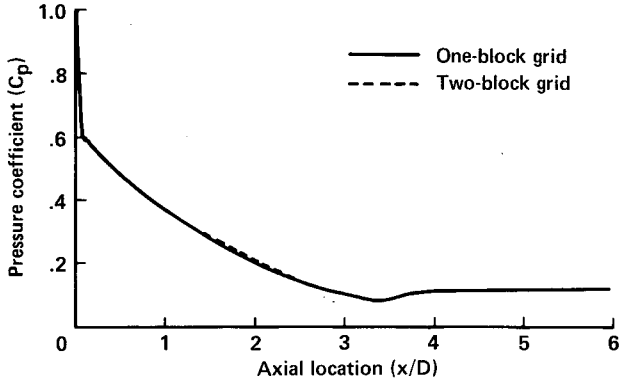

Fig. 9 Longitudinal surface pressure distributions; $M_\infty = 0.2$, $\alpha = 20$ deg, $= Re_D = 5.0 \times 10^6$ (turbulent flow).

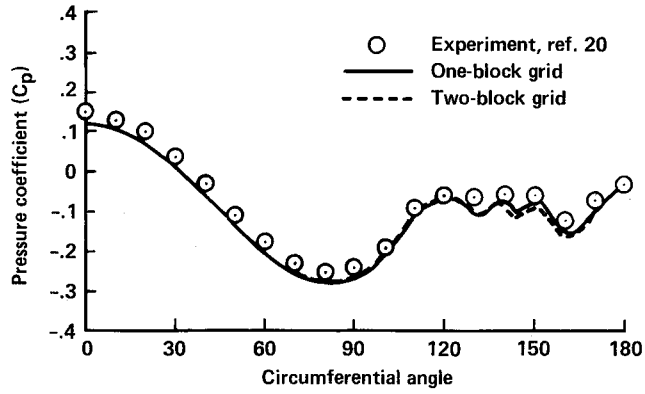

Fig. 10 Circumferential surface pressure distributions at $x/D = 6.0$; $M_\infty = 0.2$, $\alpha = 20$ deg, $Re_D = 5.0 \times 10^6$ (turbulent flow).

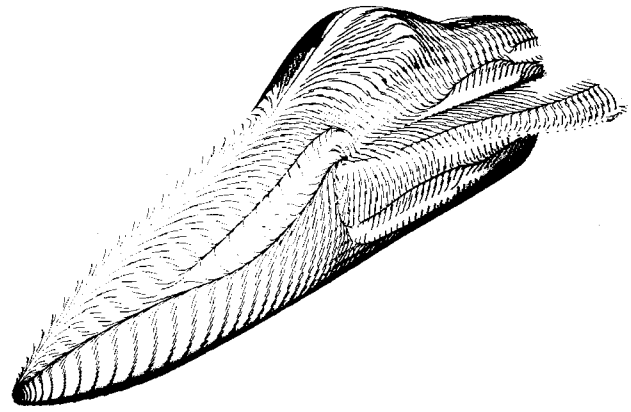

Fig. 11 Surface flow pattern on F-18—two-block grid; $M_\infty = 0.2$, $\alpha = 30$ deg, $Re_c = 806{,}400$ (laminar flow).

described earlier was used. In this case, both the front and rear grid blocks had the same number of circumferential points, and no circumferential interpolation was required. Here, the interblock boundary condition is fully flux-conservative.

The results obtained with the two-block grid are very similar to those computed with the single-block grid. Axial and circumferential surface pressure distributions for both grids, analogous to those shown in Figs. 6 and 7, are presented in Figs. 9 and 10, respectively. The windward-side axial pressure distributions (Fig. 9) indicate that the flows are in good agreement, even in the vicinity of the zonal interface. Further, as mentioned above, the circumferential pressure distributions (Fig. 10) are compared at the rear of the body in a region where large crossflow separation exists, and where the computed flows are sensitive to small changes. Despite this, the two solutions are in very close agreement. The two-block surface flow pattern is almost identical to that obtained with the single-block grid (Fig. 8). Note that in Ref. 28 a two-block solution was presented that showed discrepancies compared to the single-block solution, particularly in the circumferential pressure distribution. Consequently, the two-block solution was re-computed, and the resulting solution (Figs. 9 and 10) is in much closer agreement with the single-block results and with the experimental data. We believe that the discrepancies of Ref. 28 were caused by lack of full convergence of the previous two-block solution.

Laminar Flow Predictions for the F-18

To give perspective to the turbulent flow results, and to enable qualitative comparisons with experimental data obtained in the Langley basic aerodynamic research tunnel (BART),[29] computations were carried out for laminar flow over the F-18 fuselage forebody. The flow was computed for $M_\infty = 0.2$, $\alpha = 30$ deg, and the Reynolds number (based on mean aerody-

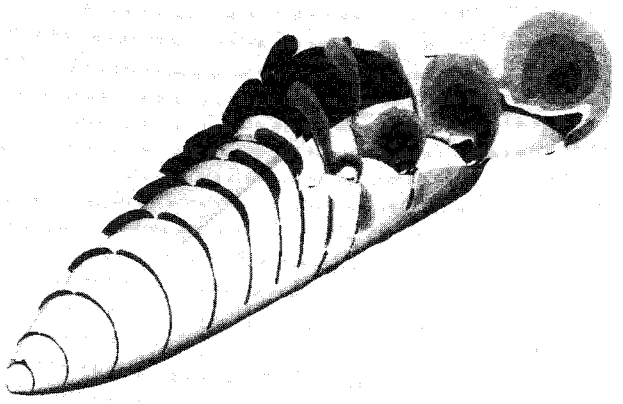

Fig. 12 Helicity density contours on F-18—two block grid; M_∞ = 0.2, α = 30 deg, $Re_{\bar{c}}$ = 806,400 (laminar flow).

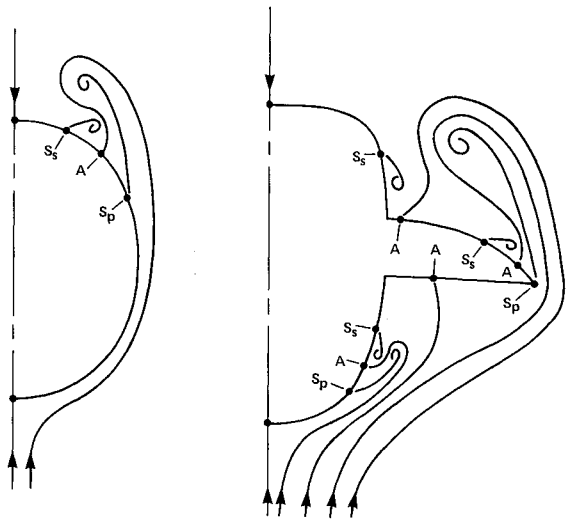

a) Upstream of LEX origin **b) Downstream of LEX origin**

Fig. 13 Schematic representation of flow structure in crossflow planes.

namic chord) $Re_{\bar{c}}$ = 806,400 using the two-block grid. The resulting surface flow pattern is presented in Fig. 11, while corresponding computed helicity density contours are shown in Fig. 12. Helicity density is defined as the scalar product of the local velocity and vorticity vectors. Since it indicates both the strength and sense of rotation of the vortices, helicity density has been found to be an excellent means of visualizing the vortex pattern.[27]

The computed flow pattern shows many of the qualitative features that were found for the simpler ogive-cylinder body. A primary crossflow separation line can be seen on the fuselage forebody upstream of the origin of the LEX. A secondary crossflow separation line begins to form approximately halfway between the nose and the LEX. The associated forebody vortices can be seen in the helicity density contours (Fig. 12).

The flow structure on the rear part of the fuselage is more complex. Flow separates circumferentially at the LEX leading edge and rolls up to form strong primary LEX vortices. The primary LEX vortex induces a flow spanwise outward on the leeward side of the LEX, which separates at a secondary crossflow separation line extending the length of the LEX. Boundary-layer fluid leaving the body along the separation line rolls up to form a secondary vortex. In addition, the primary LEX vortex induces a secondary crossflow separation on the side of the fuselage above the LEX (Fig. 12).

The flow on the windward side of the fuselage is also strongly affected by the presence of the LEX. As seen in Fig. 11, a primary crossflow separation line can be seen on the side of the fuselage under the LEX. This primary separation and its associated secondary crossflow separation are due to the circumferential adverse pressure gradient caused by the presence of the LEX. Schematic representations of the flow in two cross sections, one on the forebody upstream of the LEX, the other halfway along the LEX, are shown in Figs. 13a and 13b, respectively.

The computed surface flow pattern shows reasonable qualitative agreement with experimental surface oil flow visualizations (Fig. 14) obtained by Sellers and Kjelgaard[30] at $Re_{\bar{c}}$ = 200,000 in the basic aerodynamic research tunnel at the NASA Langley Research Center.

Turbulent Flow Predictions for the F-18

To assess the ability of the F3D code to predict high-incidence flows about aircraft at full-scale flight conditions, and to assess the suitability of the alternative computational grid topologies, several computations were carried out for turbulent flow about the F-18 fuselage forebody. These computations were obtained using both the single-block and two-block grids at flow conditions (M_∞ = 0.2, α = 30 deg, $Re_{\bar{c}}$ = 11.52 $\times$ 10^6) matching those of flight test.[31,32]

Several numerical and physical factors can affect accurate prediction of high-Reynolds-number high-incidence flow. These include the effects of numerical smoothing, turbulence modeling, and the need for sufficiently fine grids to resolve the details of both the viscous boundary and the offsurface sepa-

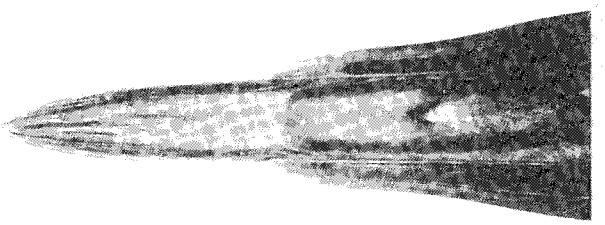

a) Top view

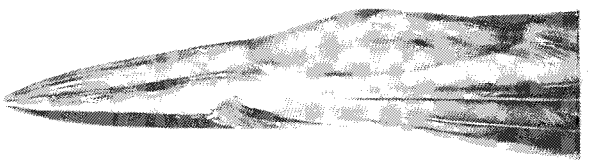

b) Top-side view

Fig. 14 Experimental oil flows from BART wind tunnel; α = 30 deg, $Re_{\bar{c}}$ = 200,000.[30]

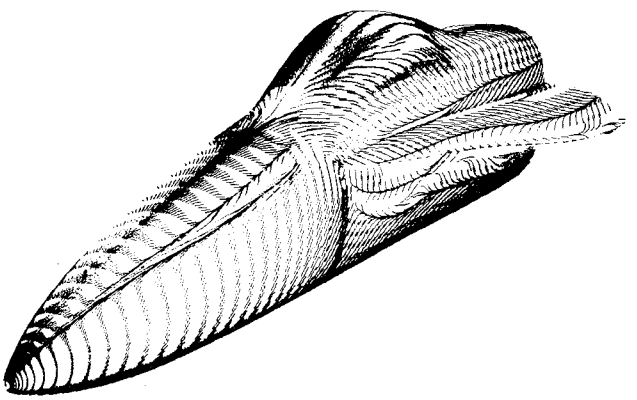

Fig. 15 Surface flow pattern on F-18—single-block grid; M_∞ = 0.2, α = 30 deg, $Re_{\bar{c}}$ = 11.52 $\times$ 10^6 (turbulent flow).

rated flow structure. A discussion of these factors for computations of flow over ogive-cylinder bodies is contained in Ref. 12. For the computations of flow over the F-18, the modified eddy-viscosity model[16] was used to model the effects of turbulence. The flow was assumed to be turbulent over the entire length of the aircraft, and no transition model was used. The radial grid spacing was chosen to give a value of $y^+ \approx 5$ at the first point above the body surface. This had been found necessary to properly resolve the viscous layer characteristics for a turbulent boundary layer.

Effect of Grid Geometry

The computed surface flow pattern and helicity density contours obtained for $\alpha = 30$ deg in the single-block F-18 grid are presented in Figs. 15 and 16, respectively. The corresponding surface flow pattern and helicity density contours obtained with the two-block grid are shown in Figs. 17 and 18.

The general features of the turbulent flows are similar to those discussed previously for the laminar flow. These include the primary and secondary crossflow separation observed on the fuselage forebody upstream of the LEX, the primary separation at the sharp LEX leading edge, and the secondary separations on the leeward side of the LEX and on the upper side of the fuselage. In addition, the solutions obtained in both grids show crossflow separation from the lower part of the fuselage due to the adverse circumferential pressure gradient caused by the presence of the LEX. The main difference observed between the computed laminar and turbulent flows is that the turbulent primary crossflow separation lines are displaced toward the leeward side of the body in comparison with the corresponding lines of the laminar flows. Also, the secondary separation line on the leeward surface of the LEX for the turbulent flow is displaced outward relative to that of the laminar case. These trends are similar to those found in a computational study of laminar and turbulent high-incidence flow over an ogive-cylinder body.[12] They occur because the turbulent viscous layer has higher momentum due to increased mixing with the adjoining inviscid flow, and can, thus, better negotiate the adverse circumferential pressure gradients.

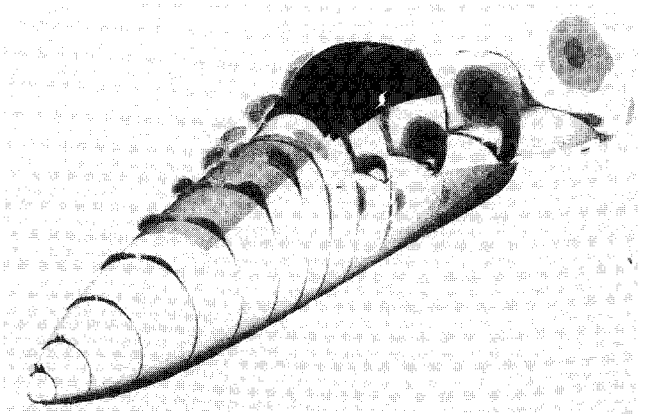

Fig. 16 Helicity density contours on F-18—single-block grid; M_∞ = 0.2, α = 30 deg, $Re_{\bar{c}} = 11.52 \times 10^6$ (turbulent flow).

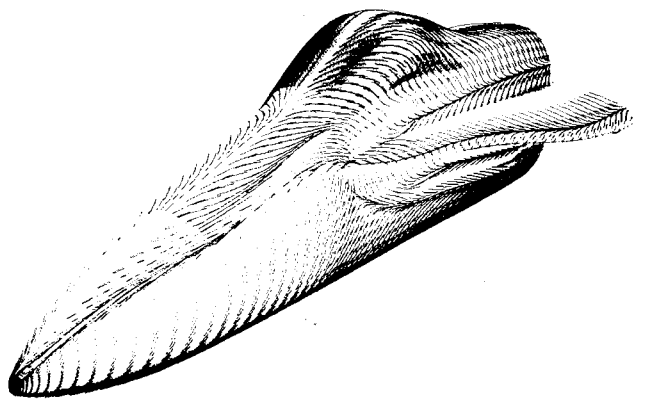

Fig. 17 Surface flow pattern on F-18—two-block grid; $M_\infty = 0.2$, α = 30 deg, $Re_{\bar{c}} = 11.52 \times 10^6$ (turbulent flow).

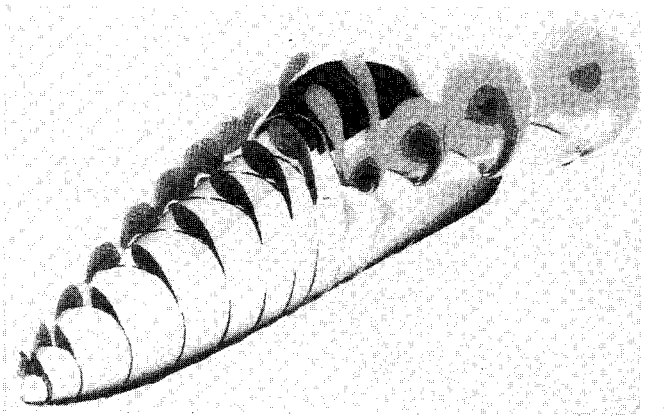

Fig. 18 Helicity density contours on F-18—two-block grid; M_∞ = 0.2, α = 30 deg, $Re_{\bar{c}} = 11.52 \times 10^6$ (turbulent flow).

The differences between the turbulent solutions obtained with the alternative grid topologies are minor (compare Fig. 18 with Fig. 16). All of the main flow features computed are similar, with only small changes observed in the positions of the lines of separation. The main difference between the two computed flows is the behavior of the forebody primary crossflow separation line just upstream of the LEX.

Comparison with Flight Tests

The computed surface flow patterns may be compared with the surface flow visualization photo, taken from flight tests conducted at the NASA Ames-Dryden Flight Research Facility,[31,32] presented in Fig. 19. This visualization, analogous to wind-tunnel oil-flow visualization, was obtained by emitting a colored solvent, propylene glycol monomethyl ether (PGME), from orifices on the aircraft surface while the aircraft was stabilized at the desired test condition. The visualization shown was obtained for $\alpha = 30$ deg and $Re_{\bar{c}} \approx 10.9 \times 10^6$. For this high Reynolds number case, the surface boundary-layer transitions from laminar to turbulent flow upstream of the first circumferential ring of dye orifices. This is confirmed by the continuous smooth behavior of the primary crossflow separation line seen in Fig. 19. Thus, the assumption that the computed flow is turbulent over the entire body length is justified.

The computed flows are seen to be in good agreement with the flight-test data, especially for the position of the primary and secondary separation lines along the forebody, and the secondary crossflow separation line along the LEX. Close agreement of the separation lines is a particularly sensitive test of the validity of the numerical method, since it involves a balance between the axial and circumferential shear stress components. Thus, good agreement with the less sensitive surface pressure measurements (to be obtained later in the flight-test program) is expected.

Existence of a crossflow separation line on the fuselage under the LEX can be inferred from the PGME flow photo (Fig. 19). This separation is of particular importance, since the resulting vortex is in a position to be ingested by the engine inlets. However, the helicity density contours (Figs. 16 and 18) indicate that the vortex is small and lies close to the side of the fuselage. In comparison, the helicity density contours indicate that the vortex originating from crossflow separation at the LEX leading edge is large and located relatively high above the LEX. A flight-test smoke-flow visualization photo[31] (Fig. 20) clearly indicates the position of the LEX vortex.

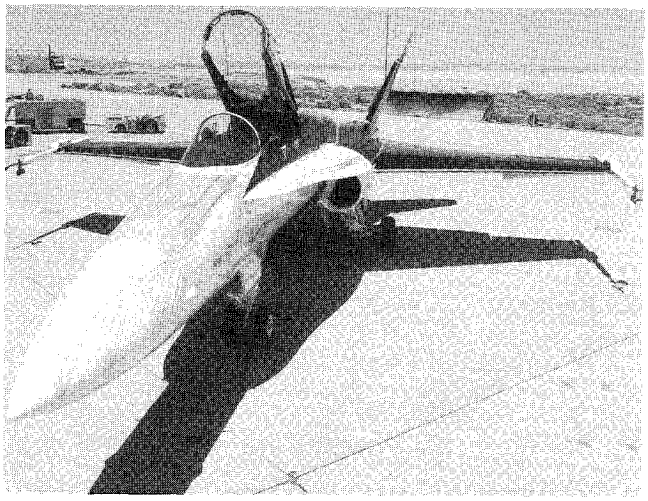

Fig. 19 Flight-test surface flow pattern; $\alpha = 30$ deg, $Re_{\bar{c}} \approx 10.9 \times 10^6$.[31]

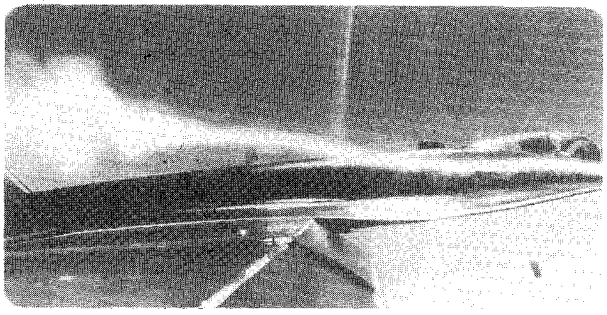

Fig. 20 Flight-test smoke-flow vortex visualization; $\alpha = 20.8$ deg.[31]

It should be noted that the computed solutions presented here do not show evidence of vortex breakdown. However, the flight-test results indicate that vortex breakdown is observed at the wing midchord for $\alpha \approx 20$ deg (see Fig. 20), and progresses forward with increase in the angle of attack, reaching the midstation of the LEX at $\alpha = 30$ deg. The reason that the predicted results do not show evidence of vortex breakdown is that the wing and aft-fuselage geometry is not included in this computation. It is expected that including this additional geometry in the computation and computing the associated adverse pressure gradient caused by the flow turning streamwise behind the wing will cause breakdown to occur, as was observed in computations[8] of flow over a slender delta wing at incidence.

Conclusions

Numerical predictions for high-angle-of-attack flow have been performed using a thin-layer Navier-Stokes code, F3D, for subsonic laminar and turbulent flow about an ogive-cylinder body and the isolated F-18 fuselage forebody. The computed results have been shown to be in good agreement with available wind-tunnel and flight-test flow visualization and surface pressure measurements, and give information about the behavior of the three-dimensional separated and vortical flow. Several factors have been found to have an impact on the ability to accurately predict high-angle-of-attack flow: 1) the turbulence model must account for the complex vortical structures found in the highly separated flow region, 2) the grid spacing must be judiciously chosen in order to insure that the salient surface and offsurface flow structures are resolved, and 3) the numerical smoothing must be used cautiously.

Acknowledgments

The authors would like to thank Ken Gee for his assistance in preparing the graphical representations of the computed flows.

References

[1]Thomas, J. L., Walter, R. W., Reu, T., Ghaffari, F., Weston, R. P., and Luckring, J. M., "A Patched-Grid Algorithm for Complex Configurations Directed Towards the F-18 Aircraft," AIAA Paper 89-0121, Jan. 1989.

[2]Ghaffari, F., Luckring, J. M., and Thomas, J. L., "Navier-Stokes Solutions About the F-18 Forebody-Strake Configuration," AIAA Paper 89-0338, Jan. 1989.

[3]Fujii, K., and Obayashi, S., "Computations of Three-Dimensional Viscous Transonic Flows Using the LU-ADI Factored Scheme," Japanese National Aerospace Lab., TR-889T, Tokyo, Japan, 1985.

[4]Newsome, R. W., and Adams, M. S., "Numerical Simulation of Vortical-Flow over an Elliptical-Body Missile at High Angles of Attack," AIAA Paper 86-0559, Jan. 1986.

[5]Pan, D., and Pulliam, T. H., "The Computation of Steady Three-Dimensional Separated Flows over Aerodynamic Bodies at Incidence and Yaw," AIAA Paper 86-0109, Jan. 1986.

[6]Kordulla, W., Vollmers, H., and Dallmann, U., "Simulation of Three-Dimensional Transonic Flow with Separation Past a Hemisphere-Cylinder Configuration," *Applications of Computational Fluid Dynamics in Aeronautics,* AGARD CPP-412, Paper 31, April 1986.

[7]Ying, S. X., Schiff, L. B., and Steger, J. L., "A Numerical Study of Three-Dimensional Separated Flow Past a Hemisphere-Cylinder," AIAA Paper 87-1207, June 1987.

[8]Fujii, K., and Schiff, L. B., "Numerical Simulation of Vortical Flows Over a Strake-Delta Wing," AIAA Paper 87-1229, June 1987.

[9]Vatsa, V. N., Thomas, J. L., and Wedan, B. W., "Navier-Stokes Computations of Prolate Spheroids at Angle of Attack," AIAA Paper 87-2627, Aug. 1987.

[10]Hartwich, P. M., and Hall, R. M., "Navier-Stokes Solutions for Vortical Flows Over a Tangent-Ogive Cylinder," AIAA Paper 89-0337, Jan. 1989.

[11]Steger, J. L., Ying, S. X., and Schiff, L. B., "A Partially Flux-Split Algorithm for Numerical Simulation of Unsteady Viscous Flows," *Proceedings of a Workshop on Computational Fluid Dynamics,* Univ. of California at Davis, Davis, CA, 1986.

[12]Schiff, L. B., Degani, D., and Cummings, R. M., "Numerical Simulation of Separated and Vortical Flows on Bodies at Large Angles of Attack," *Numerical and Physical Aspects of Aerodynamic Flows IV,* edited by T. Cebeci, Springer-Verlag, New York, 1990, pp. 205–222.

[13]Viviand, H., "Conservative Forms of Gas Dynamics Equations," *La Recherche Aérospatiale,* Vol. 1, Jan.–Feb. 1974, pp. 65–66.

[14]Baldwin, B. S., and Lomax, H., "Thin-Layer Approximation and Algebraic Model for Separated Turbulent Flows," AIAA Paper 78-0257, Jan. 1978.

[15]Steger, J. L., "Implicit Finite-Difference Simulation of Flow About Arbitrary Two-Dimensional Geometries," *AIAA Journal,* Vol. 16, No. 7, 1978, pp. 679–686.

[16]Degani, D., and Schiff, L. B., "Computation of Turbulent Supersonic Flows Around Pointed Bodies Having Crossflow Separation," *Journal of Computational Physics,* Vol. 66, Sept. 1986, pp. 173–196.

[17]Cebeci, T., Smith, A. M. O., and Mosinkis, G., "Calculation of Compressible Adiabatic Turbulent Boundary Layers," *AIAA Journal,* Vol. 8, No. 11, 1970, pp. 1974–1982.

[18]Steger, J. L., and Warming, R. F., "Flux Vector Splitting of the Inviscid Gasdynamic Equations with Applications to Finite-Difference Methods," *Journal of Computational Physics,* Vol. 40, April 1981, pp. 263–293.

[19]Ying, S. X., "Three-Dimensional Implicit Approximately Factored Schemes for Equations in Gasdynamics," Ph.D. Dissertation, Stanford Univ., Stanford, CA, 1986.

[20]Lamont, P. J., "The Complex Asymmetric Flow Over a 3.5D Ogive Nose and Cylindrical Afterbody at High Angles of Attack," AIAA Paper 82-0053, Jan. 1982.

[21]Degani, D., and Schiff, L. B., "Numerical Simulation of the Effect of Spatial Disturbances on Vortex Asymmetry," AIAA Paper 89-0340, Jan. 1989.

[22]Steger, J. L., and Rizk, Y. M., "Generation of Three Dimensional Body Fitted Coordinates Using Hyperbolic Partial Differential Equations," NASA TM 86753, June 1985.

[23]Sorenson, R. L., "Three-Dimensional Zonal Grids About Arbitrary Shapes by Poisson's Equation," *Numerical Grid Generation in Computational Fluid Mechanics '88,* Pineridge Press, Swansea, Wales, UK, 1988, pp. 75–84.

[24]Flores, J., and Chaderjian, N. M., "The Numerical Simulation of Transonic Separated Flow about the Complete F-16A," AIAA Paper 88-2506, June 1988.

[25]Reznick, S., "Transonic Navier-Stokes Computations of Strake-Generated Vortex Interactions for a Fighter-Like Configuration," NASA TM 100009, Feb. 1988.
[26]Schiff, L. B., Degani, D., and Gavali, S., "Numerical Simulation of Vortex Unsteadiness on Slender Bodies of Revolution at Large Incidence," AIAA Paper 89-0195, Jan. 1989.
[27]Levy, Y., Seginer, A., and Degani, D., "Graphical Representation of Three-Dimensional Vortical Flows by Means of Helicity Density and Normalized Helicity," AIAA Paper 88-2598, June 1988.
[28]Schiff, L. B., Cummings, R. M., Sorenson, R. L., and Rizk, Y. M., "Numerical Simulation of High-Incidence Flow over the F-18 Fuselage Forebody," AIAA Paper 89-0339, Jan. 1989.
[29]Sellers, W. L., III, and Kjelgaard, S. O., "The Basic Aerodynamic Research Tunnel—A Facility Dedicated to Code Validation," AIAA Paper 88-1997, May 1988.
[30]Sellers, W. L., III, and Kjelgaard, S. O., private communication, 1988.
[31]Fisher, D. F., and Meyer, R. R., Jr., "Flow Visualization Techniques for Flight Research," NASA TM 100455, Oct. 1988.
[32]Fisher, D. F., Richwine, D. M., and Banks, D. W., "Surface Flow Visualization of Separated Flows on the Forebody of an F-18 Aircraft and Wind-Tunnel Model," NASA TM 100436, June 1988.